Stochastic estimation of a separated-flow field using wall-pressure-array measurements

Laura M. Hudy and Ahmed Naguib[a]
Michigan State University, East Lansing, Michigan 48824

William M. Humphreys
NASA Langley Research Center, Hampton, Virginia 23681

Concurrent, surface-pressure and planar, particle image velocimetry (PIV) measurements were obtained in the separating/reattaching flow region downstream of an axisymmetric, backward-facing step at a Reynolds number of 8081, based on step height. The surface-pressure and PIV measurements were used to investigate the evolution of coherent structures in the flow field by employing proper orthogonal decomposition (POD) and multipoint, linear, stochastic estimation (mLSE) analysis techniques. POD was used to determine the dominant modes in the pressure signature, while mLSE was used to estimate the dominant flow structures above the wall from the wall-pressure POD modes over a series of time steps. It was found that a large-scale, coherent structure develops in place (i.e., *temporally*) at approximately half the reattachment distance. Once this structure reaches a height equivalent to the step, it sheds and accelerates downstream. This growth in place, and then shedding, resembles the evolution of the flow structure in the wake of bluff bodies. Such a "wake mode" has been observed in numerical-simulation studies of long cavities and backward-facing steps, where flow two dimensionality is controllable. The present study shows for the first time evidence for the existence of a wake mode in an experimental study of a backward-facing step. This is believed to relate to the quality of the two dimensionality (i.e., axisymmetry) of the test geometry and the ability to track the temporal evolution of structural features through mLSE. © *2007 American Institute of Physics*. [DOI: 10.1063/1.2472507]

INTRODUCTION

One important class of fluid flow that is encountered frequently in engineering applications is separated flows. These applications include flow over airplane wings, in dump combustors, and through turbines and compressors, to mention a few. Extensive research has been done in the area of separated flows in order to understand the dominant flow structures in the separated shear layer and the general characteristics of the flow field. Some of the research has been focused on understanding the flow generation mechanisms of wall-pressure fluctuations, which are important in engineering applications involving flow-induced noise/vibrations and flow-structure interaction. The ability to understand these and other flow physics concerning separated flows can lead to the development of simplified models for prediction of wall-pressure fluctuations and the implementation of active or passive flow control techniques for optimizing the flow state above the surface and/or minimizing the adverse flow effects on the wall.

Most of the separating/reattaching flow research to date has been on "two-dimensional" (2D) flows in *planar* canonical geometries such as a backward-facing step (BFS) (see Fig. 1 for definition of the geometry and associated coordinate system), a splitter plate, or a splitter plate with fence. Classic studies of these geometries include, but are not exclusive to, Eaton and Johnston[1] (BFS), Cherry *et al.*[2] (splitter plate), Castro and Haque[3] (splitter plate with fence), and many others. In these studies, mean-flow two dimensionality was assumed due to the large aspect ratio (width of the model divided by the step height). Since the geometries were not infinitely wide and ended abruptly at the sidewalls, the effects of the sidewalls resulted in the mean flow inherently not being two dimensional. The present research project investigates the separating/reattaching flow over an axisymmetric, backward-facing step. In the case of the axisymmetric configuration, there are no sidewall effects due to invariance in the azimuthal direction. In addition, most of the existing studies focused on understanding the general characteristics of the flow field using either surface-pressure and/or velocity measurements, while the present investigation employs both type of measurements simultaneously.

One of the few studies that looked at the velocity-field *and* surface-pressure measurements in a separating/reattaching flow geometry was Lee and Sung.[4] In 2002, they investigated the spatiotemporal characteristics of the wall-pressure fluctuations of the separating/reattaching flow region downstream of a planar, backward-facing step with Reynolds number based on a step height of $Re_h = 33\,000$. The authors used a one-dimensional (1D) array of 29 electret condenser microphones spaced over nine step heights in the streamwise direction, starting two step heights downstream of the separating edge. Pressure measurements were simultaneously acquired with velocity measurements using two

―――――――――
[a]Author to whom correspondence should be addressed. Telephone: (517) 432-1616. Fax: (517) 353-7179. Electronic mail: naguib@egr.msu.edu
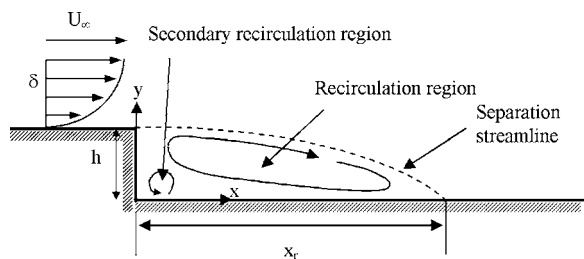
FIG. 1. Illustration of the separated flow in a backward-facing step.

split-film probes traversed over a grid of 37×21 measurement locations that extended over $2.0 \leq x/h \leq 11.0$ and $0.01 \leq y/h \leq 1.6$

The simultaneous, pressure-velocity measurements were used to analyze the interrelation between the flow field above the surface and the pressure signature on the surface. Lee and Sung[4] obtained the cross correlation of both u' and v' (streamwise and wall-normal, turbulent velocity components, respectively) with the pressure signature at zero time delay. Results from the cross correlation between the pressure and $u'(R_{u'p'})$ showed a main positive peak inclined at a negative angle with two similar negative peaks on either side. On the other hand, $R_{v'p'}$ exhibited a negative correlation peak that was located directly above the pressure position with a positive peak on either side. The highest correlation was found near the streamwise location of the wall-pressure microphone. In addition, these simultaneous measurements were used to reconstruct the flow field by conditionally averaging the velocity measurements based on specific wall-pressure conditions that were obtained from a new wave number filtering technique. The reconstructed flow field showed a well-organized, spanwise, vortical structure with $0.6U_\infty$ convection speed.

In the present study, wall-pressure-based, conditional averages of the velocity field are obtained using stochastic estimation (SE). Most of the existing SE studies have utilized velocity measurements at one or more points in the flow field to estimate the flow velocity elsewhere (e.g., Adrian,[5] Tung and Adrian,[6] Guezennec,[7] Cole and Glauser,[8] and Stokes and Glauser[9]). In 2001, a study by Naguib *et al.*[10] was the first study to use SE to estimate the flow field from the wall-pressure signature in order to determine the wall-pressure flow sources associated with surface-pressure events in a turbulent boundary layer. Simultaneous microphone and hot-wire measurements were acquired over a Reynolds number range of $1437 \leq \mathrm{Re}_\theta \leq 5670$, based on momentum thickness. The velocity measurements were obtained in the buffer and logarithmic regions of the flow field. The study estimated the velocity above the surface using both linear and quadratic stochastic estimation (LSE and QSE, respectively). Results showed that it was necessary to include the quadratic term for estimating the flow field as LSE did not capture the conditional average accurately, but the quadratic estimate showed good representation.

Taylor and Glauser[11] were the first to employ wall-pressure-array data for stochastic estimation of the velocity field of a separating and reattaching flow. The study, which examined the flow over a backward-facing ramp under varying streamwise pressure-gradient conditions, demonstrated the ability of surface-pressure measurements to properly estimate the mean flow and the low-frequency flow unsteadiness. However, the measurements did not capture the detailed evolution of the separating-shear-layer vortex structures.

In 2003, Murray and Ukeiley[12] used stochastic estimation models for resolving the temporal evolution of the velocity field above the surface from surface-pressure information in a 2D, open-cavity flow. The authors generated their surface-pressure and velocity data using numerical simulation in order to test the ability of SE to estimate the flow structures in a separating-flow geometry. They found that the linear estimate was able to predict the majority of the flow field, but that adding the quadratic term was necessary to accurately represent the turbulent energy and capture the finer details of vorticity. Finally, the authors were able to time resolve the flow evolution using SE and noted that the quadratic estimate predicted the dominant features in the flow very well when compared to the instantaneous simulated data.

A number of other investigations that employed multipoint, pressure-based, stochastic estimation have been reported in the literature. Examples include the recent work of Tinney *et al.*[13] (and references therein) who utilized the near-field pressure to estimate the flow structure in an axisymmetric jet, and studies cited in the review paper by Bonnet *et al.*[14] Because these studies do not specifically pertain to a separating/attaching flow field, they are not discussed here in detail. However, the interested reader is encouraged to consult these studies for a complete understanding of the strength and limitation of the use of stochastic-estimation-based tools to capture the flow structures associated with pressure generation.

The objective for the present study is to identify the flow structures that generate the surface-pressure signature using wall-pressure-based, multipoint, linear, stochastic estimation. Based on the instantaneous, spatial-pressure distribution, proper orthogonal decomposition is also used to highlight the dominant mode shapes in the pressure signature. These dominant signatures are then used along with stochastic estimation to explore the time evolution of the large-scale flow structures that are linked to the wall-pressure-generation process within the shear layer and downstream of reattachment.

EXPERIMENTAL APPARATUS, INSTRUMENTATION, AND MEASUREMENT TECHNIQUES

The present experiment was completed in the Subsonic Basic Research (Wind) Tunnel (SBRT) at NASA Langley Research Center in Hampton, VA. The open-circuit, low-speed, wind tunnel has a 6:1 contraction ratio upstream of a 0.57-m-wide by 0.84-m-high by 1.85-m-long test section. An adjustable false floor was placed in the test section and was set at a slight angle so that the pressure gradient in the test section was zero. The nominal height of the test section with the false floor installed was 0.62 m. The axisymmetric, backward-facing-step model shown in Fig. 2 was centered
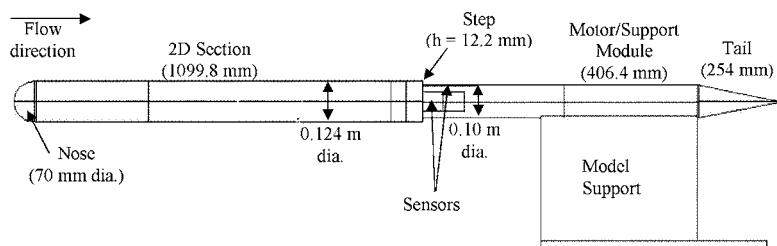
FIG. 2. Axisymmetric backward-facing-step model.

between the sidewalls, the ceiling, and the false floor within the test section.

The model measures 2.37 m in length, 0.124 m in diameter upstream of the step, and 0.10 m in diameter downstream of the step. The height of the step is 12.2 mm. Figure 2 shows a side view of the model and the labels for various components including the nose, 2D section, step, support, and tail modules. At the upstream end of the 2D section, sandpaper was used to hasten the boundary-layer transition to a turbulent state. Approximately 0.37 m or 30 step heights ($6.7x_r$, where x_r is the mean reattachment length) downstream of the step is a steel support module, which was employed to connect the model to the support stand as shown in Fig. 2. In addition, four stretches of piano wire threaded through the nose of the model and secured near the four corners of the test section were used to support the front end of the cantilever-beam-like model. Finally, at the aft end of the model, a conical tail prevents an abrupt transition of the flow surrounding the model into the flow region farther downstream.

All instrumentations were stored inside the model. Downstream of the step, the model was instrumented with 32 Emkay electret condenser microphones and 56 static-pressure taps as shown in Fig. 3. Each microphone had a nominal sensitivity of -53 ± 3 dB (relative to 10 V/Pa) over the frequency range of 100–10 000 Hz. Since the frequency range of interest extended below 100 Hz, and to account for variations in the response of individual units, the microphones were bench calibrated between 20 and 15 000 Hz using a B&K 4226 multifunctional calibrator. The 32 Emkay microphones were embedded in the surface of the model on the top side and were used to measure the unsteady pressure along the surface of the model beneath the separating/reattaching shear layer. The static-pressure taps were located on the top (one tap next to each microphone), sides, and bottom of the model and were used to characterize the mean flow surrounding the model and to align the model in the
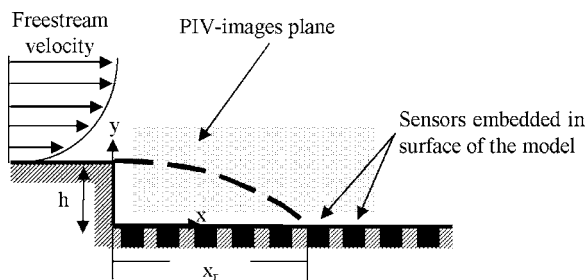
wind tunnel. The streamwise extent of the microphone and tap arrays, starting from the step, measured 153.6 mm ($12.6h$).

Simultaneously with the microphone-array measurements, planar PIV was used to measure two velocity-field components over a plane parallel to the x and y axes and located along the centerline of the model, as shown in Fig. 3. The PIV system used consisted of two MegaPlus ES-1.0, high-resolution, charge-coupled device (CCD) cameras (1018×1008 pixels) by Redlake and two Nd:YAG lasers. Surface-pressure power spectra verified that the lasers did not induce a noise signal in the microphone signature at the laser repetition frequency of 10 Hz or its harmonics even though the laser sheet was located directly above the microphones. The flow field was seeded using a pharmaceutical-grade mineral oil dispersed using a commercially available smoke generator. The mean-aerodynamic size of a particle was approximately 0.2–0.4 μm. This particle size was found to scatter enough light to be imaged by the CCD cameras and ensure that each image contained a sufficient amount of seeding to accurately cross correlate particles within the interrogation region.

To synchronize the microphone and PIV acquisition, a master signal and a steady 5-V transistor-transistor logic (TTL) pulse train were utilized. The timing diagram for the synchronization is shown in Fig. 4. Initially, both the microphone and the PIV acquisition systems were armed to start acquiring once they receive an external trigger signal. Second, two signals (a "master" and "external-trigger" signals) were sent out from a digital-to-analog (D/A) board installed in a Dell PC laptop and controlled by a LABVIEW program. The master signal consisted of a *single* 1-ms pulse given 5 ms into the start of the generation of the D/A output as shown in Fig. 4. This single pulse triggered the microphone

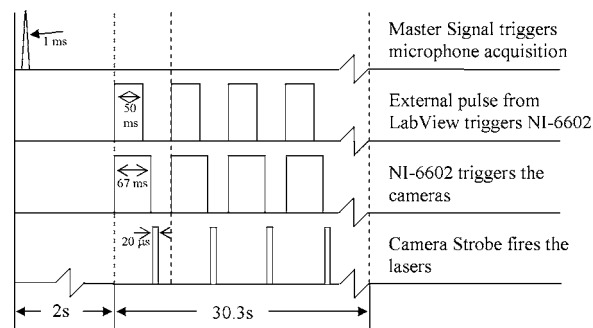FIG. 3. Measurement region for present experiment.

FIG. 4. Timing diagram for signals used to synchronize the PIV and wall-pressure data.

acquisition to start. The external-trigger signal started 2 s after the master pulse and was sent to the PIV system to start the image acquisition. This signal consisted of a 10-Hz, TTL, 50% duty cycle pulse train, which was employed to externally trigger an NI-6602 timer board that was used to control/synchronize all of the PIV-system functions; i.e., laser timing, camera triggering, and frame-straddling synchronization. The timing for the PIV acquisition system is detailed by Wernet.[15] The external trigger signal and the camera strobe that fired the lasers were acquired along with the microphone signals. Acquiring the external trigger provided the number of pulses sent to the NI-6602 timer board. The camera-strobe pulse train gave the pulses associated with the image acquisition, and it was used to match each image with the wall-pressure pattern acquired by the microphones at the same time as the image.

The system was operated utilizing an acquisition code written by Wernet[15] from NASA Glenn Research Center. Due to the length of the separation zone, the field of view had to be divided into two overlapping regions: one upstream and the other downstream of reattachment. The reattachment point was captured within the second region. Nonetheless, the two views have been merged to form one complete field of view. Merging the corresponding PIV images was completed before processing the vector fields. Prior to merging the PIV images, a piecewise-bilinear-dewarping technique was employed to remove perspective and optical distortions. This technique of "straightening" the images was developed for Doppler global velocimetry by Meyers.[16]

Once merged, the PIV images were processed using Wernet's PIVPROC processing code.[17] The images were processed using a multipass correlation technique with 50% overlap for enhanced spatial resolution and an initial 64 $\times$ 64 pixel integration box followed by a 32 $\times$ 32 pixel integration box for the second pass. This resulted in a vector spacing of 0.92 mm. Overall, the vector-field map covered 101.6 mm (8.33h) in the streamwise direction and 45.6 mm (3.74h) in the normal direction. Bad vectors were removed in CLEANVEC (a freeware program developed by Steven M. Soloff and Carl D. Meinhart) using a magnitude differencing scheme. On average, less than 3% of vectors across the vector field were removed. Missing vectors were replaced using a 5 $\times$ 5 Gaussian interpolation and the resulting vector field was smoothed using a 3 $\times$ 3 Gaussian box.

A total of 1500 PIV image pairs were acquired simultaneously with microphone data for a freestream velocity (U_∞) equal to 10 m/s, resulting in a Reynolds number, based on step height, of 8081. The separating-boundary-layer Reynolds number based on momentum thickness (Re_θ) was 1237 with a corresponding nondimensional momentum thickness of $\theta/h=0.153$. The reattachment distance was calculated to be $x/h=4.48$ using the forward flow probability technique; see Hudy et $al.$[18] for details.

EXPERIMENTAL RESULTS

Prior to examination of the wall-pressure-based, stochastic-estimation results, various statistics of the surface-
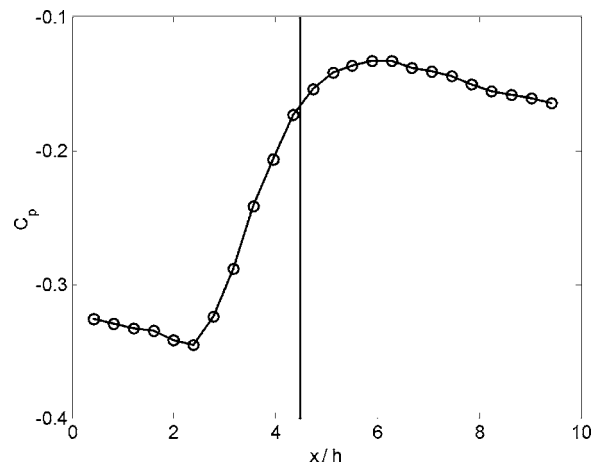

FIG. 5. Mean-pressure distribution with a line marking the x_r value.

pressure and velocity fields will be presented to demonstrate their consistency with published results.

Wall-pressure signature statistics

The mean-pressure, streamwise distribution downstream of the axisymmetric, backward-facing step is shown in Fig. 5. The mean-pressure coefficient, $C_p=(p_s-p_r)/(1/2\rho U_\infty^2)$, is plotted along the ordinate as a function of the streamwise coordinate, which is plotted on the abscissa as x/h (note that p_s is the pressure measured along the surface of the model and p_r is a reference pressure measured with a static-pressure tap located at the exit of the wind-tunnel contraction). The mean-pressure distribution shows a classical, backward-facing-step, pressure profile with mean reattachment located between $x_r=4$–$5h$. Immediately downstream of the step, the pressure distribution decreases until about $0.5x_r$, where the pressure begins to recover, reaching a peak less than two step heights downstream of x_r. The mean-pressure distribution then drops gradually as the shear layer reattaches to form a boundary layer.

The rms measurements (plotted as $C_{p'}=p'_{\mathrm{rms}}/1/2\rho U_\infty^2$) are shown in Fig. 6 as a function of x/h. A three-point average was used to smooth the rms results shown in Fig. 6 to reduce some data scatter associated with uncertainties in microphone sensitivity calibration (the largest deviation from the smoothed results is 10% with an average scatter value of about 5%). The shape of the rms distribution is consistent with that documented in the literature for a backward-facing step. At the point of separation, the shear layer is relatively far away from the wall-pressure sensors. Thus, at the first microphone location ($x/h=0.43$), a low rms pressure fluctuation is detected followed by a rapid increase of rms pressure values with increasing downstream distance from the step up to the point of reattachment, approximately. Within this region of the flow from the step to reattachment, it is believed that the surface-pressure fluctuations are predominately associated with shear-layer vortical structures. Past literature has described these structures as convecting downstream, growing in size and strength and moving closer to the wall, thus producing an increasingly strong, wall-pressure signature. This signature reaches a maximum level in the vicinity of
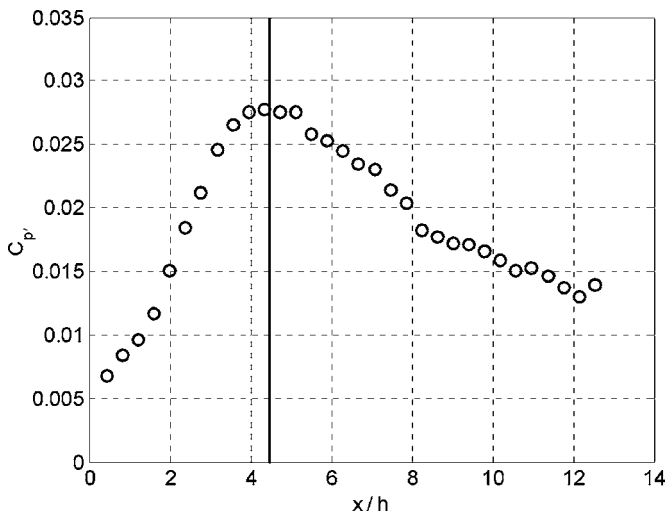
FIG. 6. rms pressure distribution with a line marking the x_r value.

where the flow "impinges," or reattaches, on the wall as described by Farabee and Casarella.[19] Beyond reattachment, the rms values slowly decrease as the energized structures from the shear layer decay and diffuse downstream in the reattached boundary layer. Similar effects were also recorded by Farabee and Casarella[19] in their planar backward-facing step study.

The rms peak in the present data occurs in the vicinity of reattachment. Heenan and Morrison[20] found their peak rms value at approximately one step height upstream of reattachment. In Fig. 6, the magnitude of the rms peak is approximately $C_{p'}=0.027$, which is comparable to the peak rms found by Farabee and Casarella[19] and Driver et al.[21] However, this value is about half the value recorded by Heenan and Morrison[20] in their planar BFS study.

Figure 7 shows a grayscale, contour plot showing the streamwise development of the surface-pressure autocorrelation ($R_{p'p'}$). Along the abscissa, the streamwise distance is normalized by the step height and along the ordinate, the correlation time shift (τ) is normalized by the freestream velocity and the step height. The grayscale bar indicates the magnitude of the autocorrelation, which is normalized by the
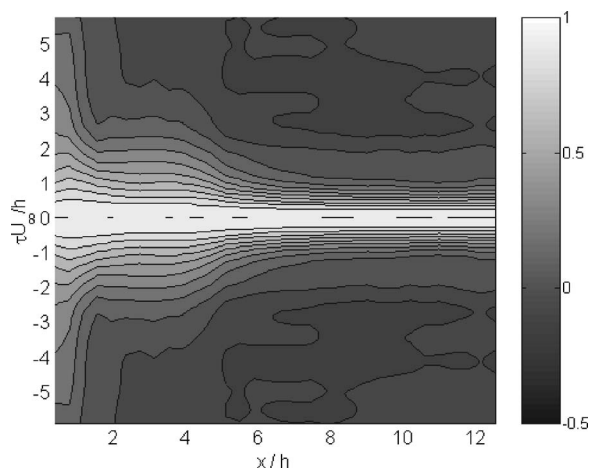
square of the wall-pressure rms to yield the correlation *coefficient* with values in the range −1 to 1.

Four distinct regions can be seen in the autocorrelation in Fig. 7 by following the zero-contour line. The first region extends from $x/h=0$, immediately downstream of the step edge, to $x/h=2$. In this region, the autocorrelation function extent is wide, indicating that the pressure signature is dominated by long-time scales, or low-frequency, flow disturbances. Other backward-facing-step studies, such as those by Eaton and Johnston,[1] Heenan and Morrison,[20] Driver et al.,[21] Farabee and Casarella,[19] and Lee and Sung,[4] have observed similar time scales near the step. Some of these studies have attributed this low-frequency dominance to the flapping of the shear layer as explained in Heenan and Morrison,[20] as well as in Eaton and Johnston.[1] Flapping refers to the unsteadiness of the shear layer trajectory, which results in variations of the reattachment point location. Equivalently, a shortening and lengthening of the separation bubble results from the flapping of the shear layer.

The second distinct region lies between $x/h=2-4$. At about $x/h=2$, the autocorrelation extent narrows, spanning $\tau U_\infty/h=-4$ to 4. The narrowing of the autocorrelation is consistent with what was observed by Hudy et al.[22] in their splitter-plate-with-fence study. In that particular study, Hudy et al.[22] found the time scales to narrow over the $x/x_r=0.25-0.5$ region, which translates to $x/h=1.12-2.24$ in the present study. The time scales for which significant correlation values exist in the present study, narrow abruptly within a shorter region than in the splitter-plate-with-fence study. As explained by Hudy et al.,[22] the narrowing of the autocorrelation extent is linked to the dominant flow structures within the shear layer. It is within this region that the flow structures are growing in strength as well as moving closer to the wall-pressure array. Thus, these higher-frequency flow structures begin to dominate the pressure signature as discussed in other backward-facing-step studies such as that by Heenan and Morrison.[20]

The autocorrelation narrows once again, starting approximately around $x/h=4$, to form the third distinct region. Within this region, which extends between $x/h=4-8$ roughly, the time scales narrow as the flow structures within the shear layer impinge on the wall at x_r and the shear layer reattaches to form a boundary layer. The fourth region starts around $x/h=8$ and continues downstream until the end of the microphone array. The autocorrelation extent within this region is the shortest compared to the other three regions. Thus, this region is dominated by the highest-frequency flow structures. It is hypothesized that the narrowing of $R_{p'p'}$ over the $x/h=4-8$ range is caused by the dominant flow structures either convecting at a faster speed and/or getting smaller in size. Beyond $x/h=8$, the contour lines remain approximately parallel to the constant τ lines showing very little change in $R_{p'p'}$ with an additional increase in x.

Figure 8 yields the cross-correlation coefficient between p' measured nearest to reattachment (specifically at $x/h=4.33$) and that measured at the locations of all 32 microphones in the array. The streamwise coordinate where the correlation is obtained is normalized by the step height and is presented along the abscissa. The normalized, correlation-
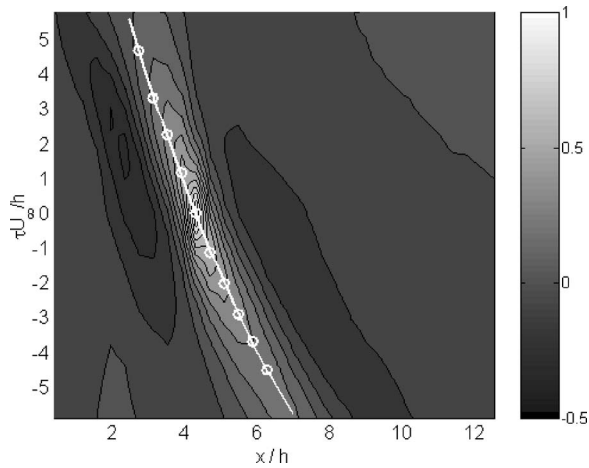

FIG. 7. Grayscale contour map of the wall-pressure autocorrelation.

FIG. 8. Grayscale contour map of the wall-pressure cross correlation (reference microphone at $x/h = 4.33$).

FIG. 9. (a) Mean-velocity vector field and (b) associated streamlines.

time delay is shown along the ordinate. The grayscale bar represents the magnitude of the cross-correlation coefficient, which was averaged over 102 records.

In Fig. 8, there is a main positive-peak lobe inclined at an angle and two negative-peak lobes on either side of the main lobe. At each x location, the main peak is centered around time shift values corresponding to the largest positive correlation between the wall-pressure signal at this x location and that near reattachment. The *slope* of the peak locus of the main positive lobe can be used to obtain an average (over all time scales) of the convection velocity (U_c) of the flow structures dominating the generation of surface-pressure fluctuations. To obtain U_c, a straight line fit of the lobe peaks (marked using open circles in Fig. 8) was attempted, but it was found that a single straight line could not fit the entire streamwise range well. Instead, a second-order polynomial (shown using a solid line in Fig. 8) provided a good fit. Because the slope of this second-order fit changes with x, it is evident that U_c is dependent on the streamwise position. This observation is discussed more in the sections below and will ultimately be linked to the physical nature of the pressure-producing flow structures.

Velocity-field statistics

Figures 9–13 show the velocity-field statistics calculated from the 1500 PIV images acquired per flow case. Statistical convergence was calculated for each quantity within the four distinct regions in the flow field: boundary layer, shear layer, freestream, and recirculating flow. It was found that the worst-case scenario (Reynolds shear-stress results within the recirculation zone) converged to within 8% based on one standard deviation. Within the shear layer, the worst convergence error was less than 3%.

Estimation of the convergence uncertainty was based on the following procedure. First, ten random locations were selected within each of the four flow regions mentioned above. For each location, subrecords extracted from the 1500 velocity fields were used to calculate the statistics for a sample size ranging from 50 to 1300 fields. The calculated statistics were normalized by their value based on a sample
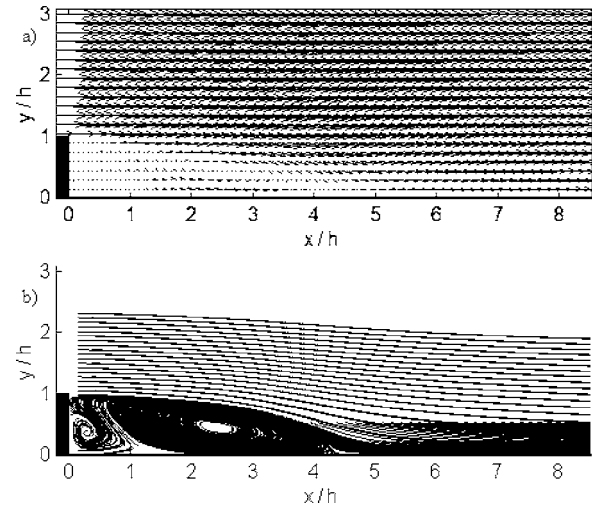
size of 1500 fields and combined with similar results from the nine other locations within the same flow region to assess the convergence. The scatter in the results for the 1300-field sample size was used as an estimate of the convergence uncertainty for the statistics based on 1500 fields.

Figure 14 shows a typical convergence plot for the Reynolds shear stress within the shear layer. The plot depicts the calculated Reynolds stress values versus the sample size. The different data points shown for a given sample size represent results obtained from different data subrecords having this size. Clearly, as the sample size increases, the number of data records available decreases. Therefore, the number of data points shown in the plot decreases with increasing sample size. As expected, the scatter in the calculated values of the Reynolds stress decreases with increasing sample size.

The velocity-field statistics in Figs. 9–13 are presented using contour maps. For the interested reader, line profiles of these statistics at selected streamwise locations that span the entire measurement domain may be found in the Ph.D. thesis of Hudy.[23] The mean-velocity vector field and associated streamlines downstream of the axisymmetric backward-facing step are shown in Fig. 9. The vector map shows a classical backward-facing-step mean-velocity field. The boundary layer separates at the edge of the step forming a shear layer that reattaches at a distance downstream of the step. The streamlines curve towards the wall with increasing x until the shear layer reattaches at x_r ($x/h = 4.48$). Beneath
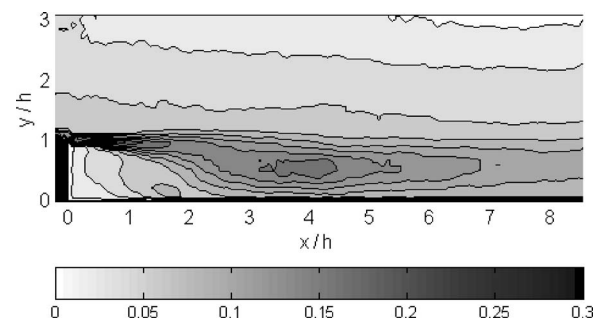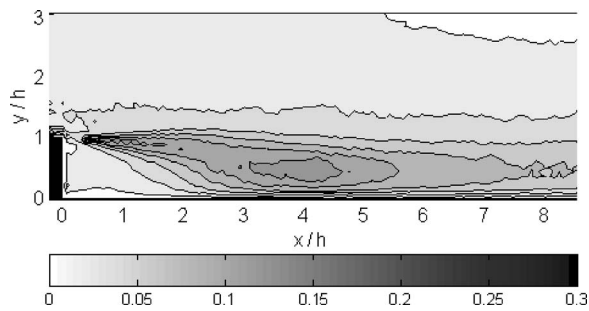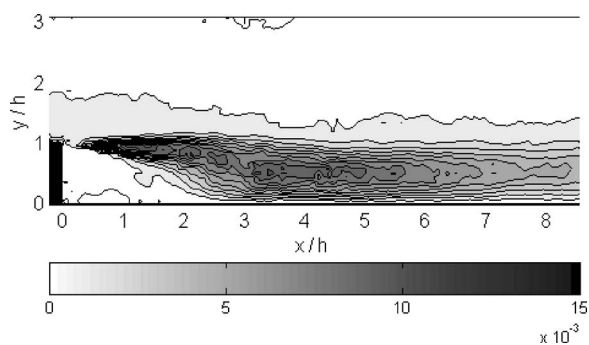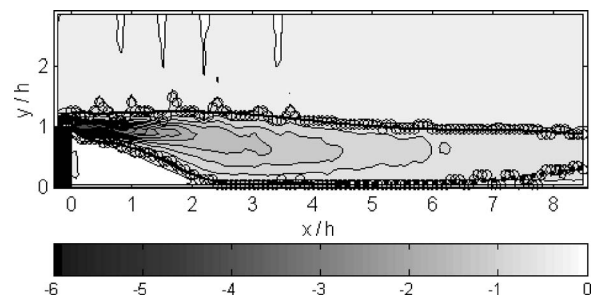

FIG. 10. Grayscale contour map of u_{rms}/U_∞.

FIG. 11. Grayscale contour map of $v_{\mathrm{rms}}/U_\infty$.

FIG. 13. Grayscale contour plot of the mean spanwise vorticity, ω_z^* $=\omega_z h/U_\infty$.

the shear layer there is a clockwise recirculation zone that stretches from $x/h \approx 1.1$ to x_r. Near the step, within the $x/h=0–1.1$ region, the streamlines indicate a secondary recirculation zone, which is a characteristic feature in BFS flows. Scarano and Riethemuller[24] along with Kostas et al.[25] were also able to capture the secondary recirculation zone in their recent PIV studies of a planar BFS. Beyond reattachment, the shear layer forms a reattached boundary layer as shown in Fig. 9.

Figures 10 and 11 show the longitudinal (u_{rms}) and vertical (v_{rms}) turbulent fluctuations. Each figure is a grayscale, contour map with the streamwise distance downstream of the step, x/h, shown along the abscissa and the distance normal to the wall, y/h, given along the ordinate. These axes will be used for all grayscale contour plots in this section. The grayscale bar on the bottom of the contour plot indicates the magnitude of the particular turbulent rms velocity normalized by U_∞. For the plots in Figs. 10 and 11, the peak root-mean-square values are located within the separating-shear layer, with the highest peak along the center of the shear layer near the separation edge. The data presented in Figs. 10 and 11 compare well, qualitatively, with Scarano and Riethmuller[24] in their PIV study of a planar, backward-facing step. In addition, the general behavior observed is consistent with the findings of Castro and Haque[3] as well as Ruderich and Fernholz[26] in their investigations of a fence-with-splitter-plate flow. Both studies employed the maximum loci in the turbulent intensity plots to determine the center of the separating-shear layer. Quantitatively, the rms magnitudes in the current study are higher than in Scarano and Riethmuller's[24] study. In particular, the u_{rms} and v_{rms} values are almost double the values found by these authors. It is

interesting to note that, in contrast to a free-shear layer, which spreads gradually and smoothly with increasing x, the reattaching, shear layer initially diverges smoothly until approximately $x/h \sim 2$ when a "sudden" divergence occurs and the shear layer grows to a thickness approximately equal to the step height. This is also the streamwise location at which the width of the wall-pressure autocorrelation reduces somewhat abruptly (see Fig. 7). The velocity rms results suggest that the transition in the wall-pressure field characteristics is associated with the shear-layer structures approaching the wall. This was hypothesized through inference using the wall-pressure data alone. The velocity-field data confirm the hypothesis. The stochastic estimation, to be shown later, will demonstrate that this "ballooning" of the shear layer near $x/h=2$ relates to the formation of large-scale (order of the step height) vortex structures near this location.

Figure 12 provides the Reynolds shear stress, $-\overline{u'v'}/U_\infty^2$ information for the axisymmetric backward-facing step in the form of a grayscale, contour map. Compared to Scarano and Riethmuller[24] and Kostas et al.,[25] who found maximum $-\overline{u'v'}/U_\infty^2$ values slightly upstream of reattachment, the intensity of the Reynolds stress values in Fig. 12 do not indicate a local peak within the shear layer near reattachment. Instead regions of high Reynolds stress are seen throughout the shear layer. Scarano and Riethmuller[24] found a peak $-\overline{u'v'}/U_\infty^2$ of 0.012 before reattachment at $x/h=2$. Kostas et

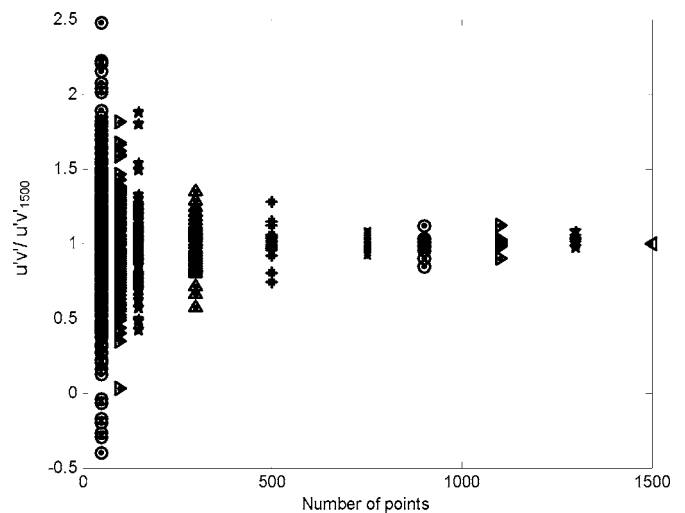FIG. 12. Grayscale contour map of $-\overline{u'v'}/U_\infty^2$.

FIG. 14. Plot used to determine the convergence uncertainty for the Reynolds-stress calculation.

al.[25] reported a value of 0.0094. The magnitude of both local peaks from these two studies is comparable to the maximum values seen in Fig. 12 of $-\overline{u'v'}/U_\infty^2 \approx 0.01$.

Finally, Fig. 13 shows the out-of plane vorticity (ω_z). The mean vorticity was calculated using the circulation-based method of Raffel et al.[27] The method relies on the fact that vorticity is related to circulation through Stokes theorem. More specifically, the *average*, area-normal vorticity within a particular area can be estimated by calculating the circulation along a contour surrounding the area and dividing the result by the enclosed area. The magnitude of the vorticity, normalized as $\omega_z^* = \omega_z h/U_\infty$, is given by the grayscale bar in Fig. 13. Finally, the solid and dashed black lines mark the point where the vorticity is 8% of the global peak vorticity. These lines were determined by finding, for each streamwise location, the vertical position at which the vorticity equaled 8% of the peak vorticity in the flow (these positions are displayed using open circles in Fig. 13). A seventh-order polynomial fit of these locations was then used to obtain the two solid black lines and a third-order polynomial fit was used for the dashed white line. The order of the polynomial was selected to provide a good fit quality and the fits are found to be good for the most part except near reattachment. The solid black line along the top of the shear layer traces the outer edge of the shear layer from the step all the way downstream. The bottom edge of the shear layer can only be traced with confidence up to reattachment. Beyond x_r, the dashed line indicates where the lower edge of the shear layer may be located. It is difficult to determine the lower edge of the shear layer beyond reattachment since, once the flow reattaches, a new boundary layer begins to develop beneath the reattached flow. The point that delineates the two regions is difficult to determine.

Looking at the mean-vorticity distribution, the concentration of substantial negative vorticity within the flow field is confined to the shear-layer region. Within the shear layer, there is a local vorticity peak seen slightly downstream of the separating edge. At this point the shear layer is the thinnest and the vorticity is the highest. The vorticity distribution grows in width in the downstream direction, and at the same time the intensity level of the vorticity decreases. The spread rate of the vorticity distribution in the wall-normal direction is particularly pronounced around $x/h=1–2$, which is consistent with the lateral spread of the distribution of the rms velocities and the Reynolds stress (Figs. 10–12). Kostas et al.,[25] who investigated the flow field downstream of a backward-facing step using PIV for $Re_h=4660$, referred to the shape as bulbous. Downstream of reattachment, the level of vorticity continues to decrease as the reattached shear layer begins to diffuse and a new boundary layer begins to develop.

Convection velocity

Figure 15 compares the convection velocity determined from the wall-pressure signature with the local, mean velocity measured at the center of the shear layer at different x locations. The convection velocity of the dominant, wall-pressure-generating, flow structures was calculated from the
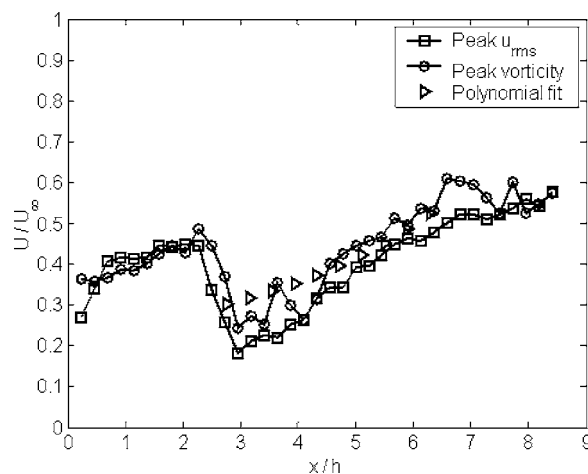

FIG. 15. Mean velocity at the shear-layer center, and average convection velocity calculated from the wall-pressure cross correlation.

second-order fit to the cross-correlation peak locus (shown as a solid line in Fig. 8). The derivative of the fit gives U_c as a function of streamwise distance as shown in Fig. 15. For the mean-velocity results, the center of the shear layer has been defined based on (1) the peak of the u_{rms}/U_∞ at each x/h location and (2) the peak of the mean vorticity at each x/h location. Figure 15 suggests that the convection velocity of the dominant, wall-pressure-generating, flow structures agrees well with the local, mean velocity at the center of shear layer. The agreement is better for the reattached boundary layer than in the shear layer region. An important point to note is that all three velocity profiles show an *acceleration* of the flow structures beyond $x/h=3$. This point will be explained in more detail in the following sections.

Single-point linear and quadratic stochastic estimation

Although the ultimate goal of this work is to employ multipoint, linear stochastic estimation to study the flow structures associated with surface-pressure generation, results from single-point estimation are examined first in order to assess the consequences of truncating the estimation at the linear term. This task is more easily accomplished through single-point analysis given the complexity of undertaking multipoint, nonlinear stochastic estimation (the reader is referred to Naguib et al.[10] and Murray and Ukeiley[12] for examples of single-point and multipoint quadratic estimations, respectively). However, once the reasonableness of the linear estimation is established, the spatiotemporal evolution of the wall-pressure-generating structures will be examined through a multipoint, linear analysis.

Resorting to the multipoint estimation for the main analysis is important given that Cole et al.[28] and Bonnet et al.,[29] among others, have demonstrated the superiority of multipoint over single-point estimation in providing a "realistic" representation of the flow field. Generally speaking, mLSE imposes a *strict spatial condition* for estimating the *conditionally averaged* flow field by using a particular, spatial-pressure-distribution condition. In contrast, LSE imposes only a pressure-value condition that could be associ-
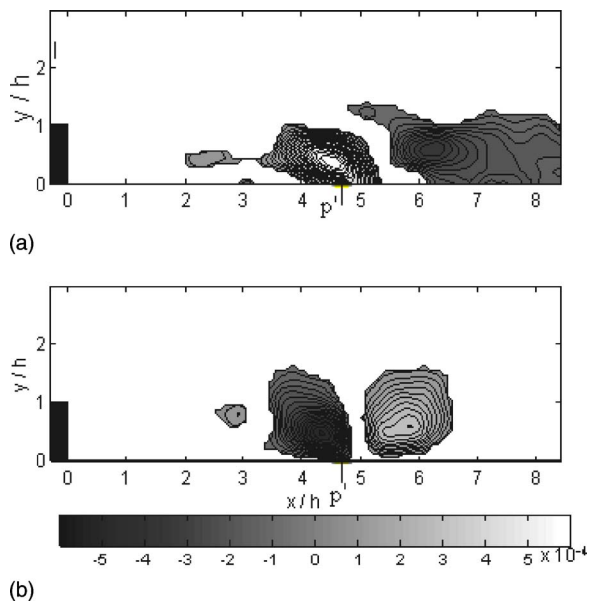
FIG. 16. Grayscale contour plots of (a) $R_{u'p'}/(1/2\rho U_\infty^3)$ and (b) $R_{v'p'}/(1/2\rho U_\infty^3)$ for pressure measurements at $x/h=4.68$.

ated with widely varying spatial patterns. Hence, with its stricter condition, mLSE is less likely to deviate from the instantaneous flow field than LSE. This would be particularly true for flow fields where the pressure generation is dominated by coherent motions.

LSE was used to estimate the u' and v' components of the velocity based on a known, wall-pressure signature according to

$$\tilde{u}'(x_o + \Delta x, y, t) = A_u(\Delta x, y; x_o)p'(x_o, t), \tag{1}$$

$$\tilde{v}'(x_o + \Delta x, y, t) = A_v(\Delta x, y; x_o)p'(x_o, t), \tag{2}$$

where $\tilde{u}'$ and $\tilde{v}'$ are the estimated streamwise and normal fluctuating velocities, respectively, x_o is the streamwise position of the known variable (wall-pressure condition), Δx is the streamwise distance between the known and estimated variables, y is the normal coordinate (also the normal distance between the known and estimated variables), t is the instant in time at which the pressure event occurs, p' is the measured fluctuating pressure on the wall, and A_u and A_v are the linear estimation coefficients for $\tilde{u}'$ and $\tilde{v}'$, respectively. Details regarding the SE technique can be found in several studies such as those by Adrian,[5] Guezennec,[7] and Stokes and Glauser,[9] to name a few.

Single-point, linear, stochastic estimation requires information from the cross correlation between the fluctuating pressure signature at one streamwise position and the fluctuating velocity field in order to determine the linear-estimation coefficient. An example of such a cross correlation is shown in Figs. 16(a) and 16(b) for the streamwise position $x/h=4.86$, which is near reattachment. Figure 16(a) shows the grayscale contour plot of the cross correlation between the fluctuating pressure at $x/h=4.68$ and the mean-removed, streamwise-velocity component (i.e., $\mathbf{R}_{u'p'}$) at ev-

ery node in the flow field. Figure 16(b) displays a similar plot for the mean-removed, normal-velocity component (i.e., $\mathbf{R}_{v'p'}$).

In Fig. 16, the streamwise coordinate is shown on the abscissa as x/h and the normal direction is plotted along the ordinate as y/h. The grayscale bar gives the magnitude of the cross correlation normalized by $(1/2\rho U_\infty^2)U_\infty$. The normalization used for the cross correlation allowed for identification of correlation regions that are strong globally (i.e., over the entire flow domain). The traditional means of normalization using the local u'_{rms} and p'_{rms} proved difficult to use to compare between the strength of the correlation at different locations in the flow because of the variation in rms values from one point to another. However, rms-based normalization is useful in judging the significance of the calculated correlation values. When normalized by local rms values, the $\mathbf{R}_{u'p'}$ and $\mathbf{R}_{v'p'}$ values fall between -0.4 and 0.4. In Fig. 16, only correlation values below/above the uncertainty level (correlation value of $\pm 0.000\,08$) are shown in order to highlight the significant correlations in the flow field (note again the apparently small values in the figure are due to normalization by the freestream velocity). Finally, an arrow with the label "p'" indicates the streamwise position for the microphone used in the correlations.

The random uncertainty of the correlation values was determined to be 10% in the worst case. The procedure for obtaining the random uncertainty was similar to that described earlier for the convergence of the velocity-field statistics. In the case of velocity-pressure correlation, the convergence tests were conducted for three representative wall-pressure measurement locations: upstream, near, and downstream of the mean reattachment point (specifically, $x/h=3.51$, 4.68, and 5.46, respectively). Also, only points in the flow field exhibiting high velocity-pressure correlation with the pressure at each of these locations were employed in determining the convergence uncertainty.

As seen in Fig. 16(a), a positive correlation peak can be seen, inclined at a slight angle, near the $x/h=4.68$ microphone location. This positive peak stretches over the range $x/h=3.5–5.4$ and $y/h=0–1.0$. A negative correlation region can also be seen in Fig. 16(a) downstream of $x/h=4.68$. It stretches over the ranges $x/h=5–8.5$ and $y/h=0–1.3$. Figure 16(b) shows the $\mathbf{R}_{v'p'}/(1/2\rho U_\infty^3)$ contour plot for the same streamwise position of wall-pressure measurements. Both a positive and a negative peak can be seen in the correlation plot; although, in opposition to the $\mathbf{R}_{u'p'}$ results, the main, negative peak is now located directly above the microphone used for the correlation, and the main, positive peak is located farther downstream. The flow structure implied by these correlations is more readily obtained from the stochastic estimation results, as given below.

Using the cross-correlation results between pressure and velocity in Fig. 16, the linear-estimation coefficients were obtained, and the flow field was estimated based on the condition that the pressure at a particular streamwise position was five times the rms. This was computed for both a negative and positive pressure event at the same streamwise as that used in obtaining the cross-correlation contour plots in Fig. 16. The mean-velocity field was then added to the esti-
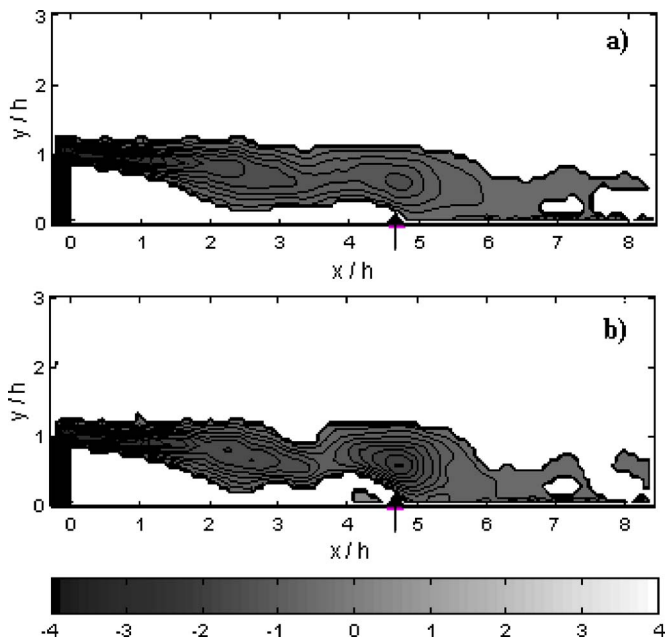
FIG. 17. Spanwise-vorticity field of the single-point stochastic estimation results for a negative pressure event ($p'=-5p_{rms}$) at $x/h=4.68$. (a) Linear and (b) quadratic results.
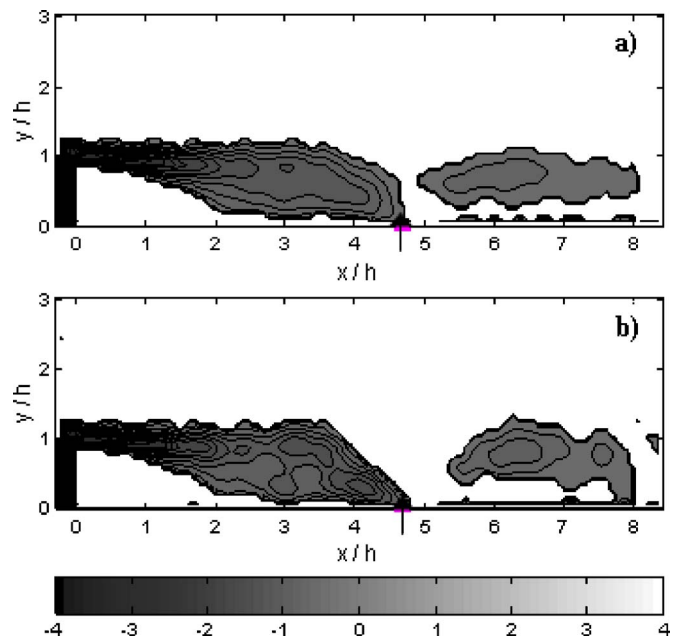

FIG. 18. Spanwise-vorticity field of the single-point stochastic estimation results for a positive pressure event ($p'=+5p_{rms}$) at $x/h=4.68$. (a) Linear and (b) quadratic results.

mated field to provide an estimation of the full flow field rather than the turbulent field alone. It is noted here that a particularly strong pressure condition is employed in order to offset the weakening of the stochastically estimated velocities relative to the mean flow due to the inherent averaging involved in the estimation. A similar procedure was also used by Ukeiley and Murray,[30] who noted that the process of scaling the estimated field helps in visualizing the flow features without changing their associated structure.

Figures 17 and 18 show the spanwise-vorticity field of the linear, stochastic estimation results. In addition, results from the quadratic stochastic estimation, which is explained in more detail below, are also shown. The vorticity from both the LSE and QSE for a negative-pressure event at $x/h=4.68$ is shown in Fig. 17 and for a positive-pressure event in Fig. 18. The grayscale bar indicates the magnitude of the normalized vorticity ($\omega_z^* = \omega_z h/U_\infty$). Vorticity levels between -0.4 and 0.4 were set at zero in order to minimize noise in the contour plots and enhance the visibility of the dominant features in the flow field.

The single-point QSE was used as a means of verifying the accuracy of the single-point LSE. QSE was used as a check to see what additional information the quadratic term provides in the flow field and, more importantly, how well does LSE estimate the flow field. The equations used to estimate the u' and v' components of the velocity based on the pressure signature using quadratic stochastic estimation are the following:

$$\tilde{u}'(x_o + \Delta x, y, t) = A_{u,\text{quad}}(\Delta x, y; x_o)p'(x_o, t) + B_u(\Delta x, y; x_o)p'^2(x_o, t), \tag{3}$$

$$\tilde{v}'(x_o + \Delta x, y, t) = A_{v,\text{quad}}(\Delta x, y; x_o)p'(x_o, t) + B_v(\Delta x, y; x_o)p'^2(x_o, t), \tag{4}$$

where $A_{u,\text{quad}}$ and $A_{v,\text{quad}}$ are the coefficients of the linear term, and B_u and B_v are the coefficients of the quadratic term in the estimation. More details regarding QSE, including the equations for the coefficients, are given in Naguib et al.[10]

In Fig. 17(a), a region of localized negative-vorticity concentration is shown directly above the microphone used in the estimation. The concentration of vorticity can be seen more clearly in the QSE results in Fig. 17(b), suggesting the presence of a vortical structure immediately on top of the point of observation of the negative pressure event. The above suggests that the generation of negative-pressure events on the wall is linked to the passage of large-scale (order h) vortical features. On the other hand, the LSE vorticity field in Fig. 18(a) shows that the estimation using a positive pressure signature at $x/h=4.68$ produces localized concentration of vorticity upstream and downstream of this streamwise position. Again, this is better defined in the QSE results in part (b) of the same figure.

Figure 19 shows the strain-rate fields from the single-point QSE results at $x/h=4.68$. Results are shown for both a negative-pressure event [Fig. 19(a)] and a positive-pressure event [Fig. 19(b)]. Only the quadratic results are shown since Hudy[23] showed that the quadratic term is needed in the estimation of strain rate. Figure 19 shows that a localized high-strain-rate region exists immediately above the positive-pressure event and upstream of the negative-pressure condition. Comparison with Figs. 17(b) and 18(b) makes it evident that the local, high-strain-rate region is located in between the two zones of high vorticity.

The above findings are consistent with the study of Naguib and Koochesfahani,[31] who found that for the flow
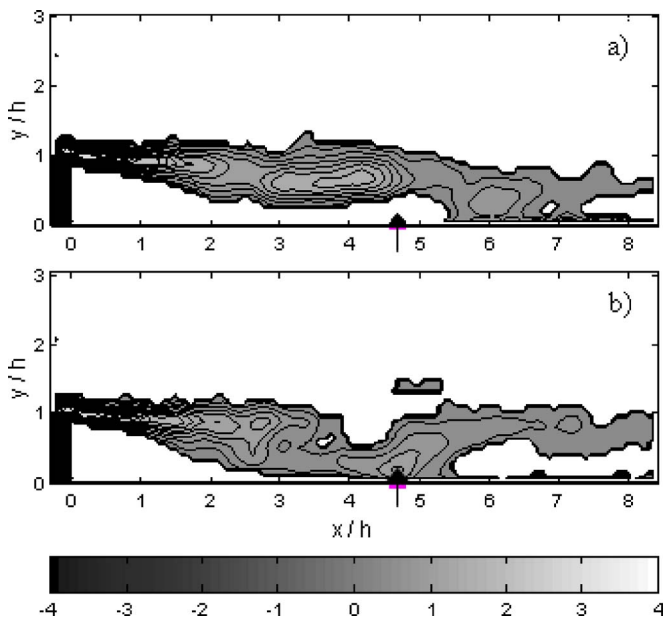
FIG. 19. Strain-rate field of the quadratic results for single-point stochastic estimation for (a) negative ($p' = -5p_{rms}$) and (b) positive pressure event ($p' = +5p_{rms}$) at $x/h = 4.68$.

field of an axisymmetric vortex ring impinging on a flat wall, strong positive-pressure generation was associated with high-strain-rate flow regions. Additionally, they identified the core of the vortex structures to be associated with strong generation of negative pressure at the wall. These findings were related to the earlier study of Bradshaw and Koh[32] in which it was shown that, in general, positive-pressure generation can be solely attributed to fluid strain while negative-pressure production arose due to vorticity.

A comparison between the LSE and QSE results for vorticity (Figs. 17 and 18) shows that the global flow features are the same as found by both techniques, but the features are enhanced and magnified by the addition of the quadratic term. LSE is able to capture the large-scale structures with some smearing, while QSE defines the details of the large-

scale structures more clearly. Since LSE captures the global features of the vorticity field well, and it is substantially simpler to implement than QSE for multipoint conditions, subsequent multipoint estimation will only employ the linear estimation. This qualitative justification for the use of the linear estimation is suitable for the purposes of the present study, where the focus is on examination of the spatiotemporal evolution of the wall-pressure-generating structures. However, in cases where it is desired to estimate the quantitative aspects of these structures (such as the associated kinetic energy, velocity spectra, etc.), nonlinear terms should generally be included in the estimation.

Instantaneous pressure signature

Although the above single-point analysis gives information regarding the flow structures associated with the generation of strong, wall-pressure events, the results are biased to one particular microphone at a single, streamwise location. This assumes that a flow structure only affects a single sensor and, therefore, only the pressure signature from that sensor is needed to reconstruct the associated flow field. In general, however, flow structures will imprint a pressure signature on multiple microphones. Additionally, it can be seen from the cross-correlation plots in Fig. 16 that the correlation between the velocity and a single wall-pressure sensor only extends over a limited part of the velocity field. Therefore, in order to estimate the flow structures over the entire flow field, it is necessary to have several sensors at various streamwise locations. The array of 32 microphones embedded in the wall of the axisymmetric backward-facing-step model enabled such multisensor analysis by measuring the pressure signature at multiple points in space.

Figure 20 shows examples of the pressure signature over all 32 microphones at different instants in time. The abscissa gives the streamwise distance and the ordinate gives the unsteady pressure in pascals. Each signature was bandpass filtered between 20 and 160 Hz ($fh/U_\infty = 0.024 - 0.19$), where the most energetic part of the pressure fluctuations is concentrated. This was found from the wall-pressure spectra in
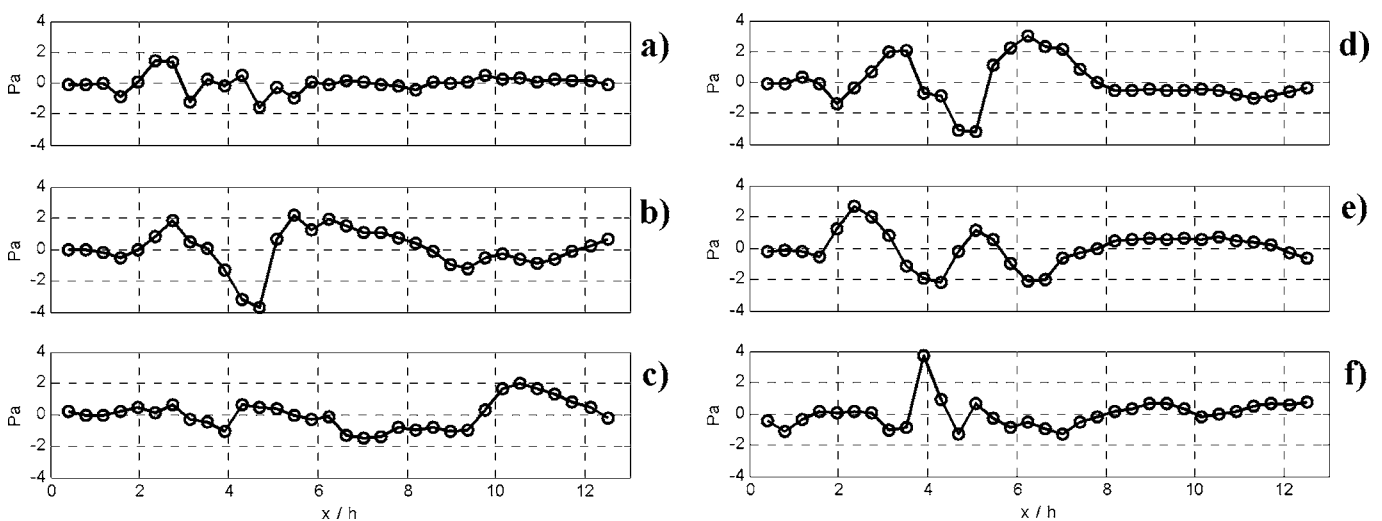

FIG. 20. Examples of measured spatial, pressure signatures at six instants of time.

Hudy,[23] who associated the pressure fluctuations in this frequency band with the passage of the shear-layer structures. Thus, the bandpass filtering allows one to focus the analysis on the flow features associated with the shear layer.

Looking at all six spatial-pressure signatures presented in Fig. 20, it can be seen that at certain instances in time, the pressure signature seems random and relatively low in magnitude, as seen in Figs. 20(a), 20(c), and 20(f). These signatures show low-pressure levels, roughly between −1 and +1 Pa, over most of the spatial extent. In addition, spatially, the pressure distribution seems unorganized compared to, for example, the signatures in Figs. 20(b), 20(d), and 20(e), where a certain level of organization, almost a modulated "sinusoidal-like" distribution, can be seen. The corresponding pressure magnitude spans a larger range (−4 to 4 Pa) than seen with the random signatures.

Similar observations were made by Cherry et al.[2] in their investigation of the flow around a thick, splitter plate at Re =32 000 based on model thickness. Two Setra 237 low-pressure transducers were mounted inside their model and were used to measure the fluctuating pressure on the wall. Smoke visualization was used to monitor the flow field simultaneously as the pressure fluctuations were acquired. From their data set, Cherry et al.[2] synchronized the pressure traces with the flow visualization and were able to describe the pressure signature in time as being associated with various shedding phases. One such phase was the shedding of pseudo, periodic trains of vortical structures from the reattachment zone. The smoke visualization showed that these structures had a characteristic spacing of approximately 60–80% of the reattachment length. Large-scale vorticity was also observed to have an irregular shedding pattern and there were quiescent periods where no large-scale shedding occurred. These quiescent periods in the flow field were found to be synchronized with periods in the pressure trace where the pressure fluctuations were random and low in magnitude. During a shedding phase, the pressure signature was found to be energetic, showing higher peaks and lower valleys (in magnitude) than in the quiescent phase.

It is evident from the pressure signatures displayed in Fig. 20 that the pressure traces measured here have characteristics that are commensurate with the observations of Cherry et al.[2] with $p'(x)$ switching in time between a quiescent, random signature and a more organized energetic phase. To focus the subsequent analysis on the energetic/coherent component of the wall-pressure signature only (specifically when estimating the flow field from the wall-pressure-array data), proper orthogonal decomposition is first applied to the surface-pressure data. POD is a mathematical technique that extracts the various mode shapes (spatial shapes) of the most energetic pressure signatures. Some background on the technique and results of its use here are given next.

Proper orthogonal decomposition (POD)

Proper orthogonal decomposition is an unbiased technique used for extracting organized signatures (or mode shapes). It was first introduced in 1967 by Lumley[33] for use
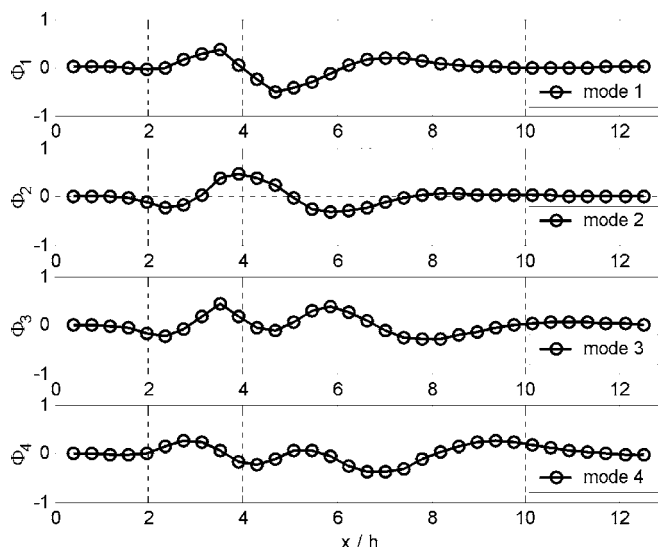

FIG. 21. First-four wall-pressure-mode shapes defined by POD.

in problems of turbulence. The technique is used to identify the more energetic structures in a flow field. The idea behind POD is that it assumes that a random field can be represented by a set of deterministic, spatial functions superposed with coefficients (or amplitudes) that are random functions of time. Fourier decomposition assumes the same ideology, except that the functions are predetermined to be sinusoidal with random amplitudes and phases. The uniqueness of POD stems from its ability to extract both the spatial functions and the associated coefficients used to define the random field based on statistical properties of the field. Interestingly, POD reduces to Fourier analysis along coordinate directions where the flow is homogenous. Therefore, the strength of POD lies in its application in directions where the flow is inhomogeneous, and therefore Fourier modes, with their infinite spatial extent are, strictly speaking, inappropriate for representing the flow. For more information regarding the background of POD and the implementation of the technique, refer to Berkooz et al.[34]

The results of the POD analysis are shown in Fig. 21, which gives the first four modal shapes $[\phi_n(x)$, where n is the mode number] plotted as a function of streamwise distance (x/h). A total of 32 modes were calculated using POD since there were 32 wall-pressure sensors. An inherent character of POD modes is that the modes are ranked in order of decreasing importance; i.e., the first mode is the most energetic, followed by the second, etc. In the present work, this means that the first mode generates the most pressure fluctuation on average, followed by the second mode, and so on. This may be seen in Fig. 22, which shows the percentage of the fluctuating-pressure-field energy recovered from the POD representation plotted versus the number of POD modes used to represent the pressure signature. Naturally, the inclusion of all 32 modes in the representation recovers 100% of the energy in the signal. However, the combination of modes 1 and 2 alone makes up almost 40% of the energy content in the signal. Modes 3 and 4 make up an additional 20%. This is significant in that 60% of the energy in the pressure signa-
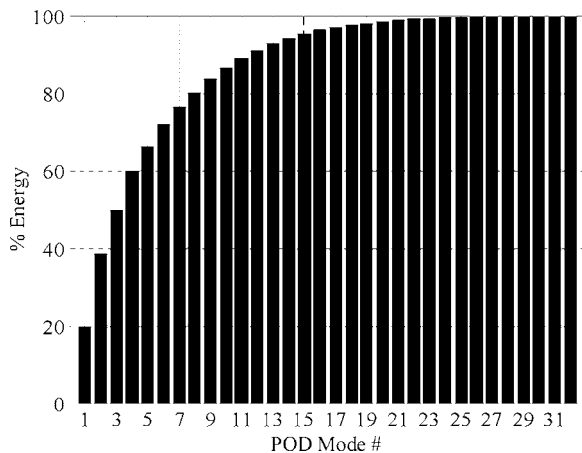
FIG. 22. Cumulative distribution of wall-pressure energy over all 32 POD modes.
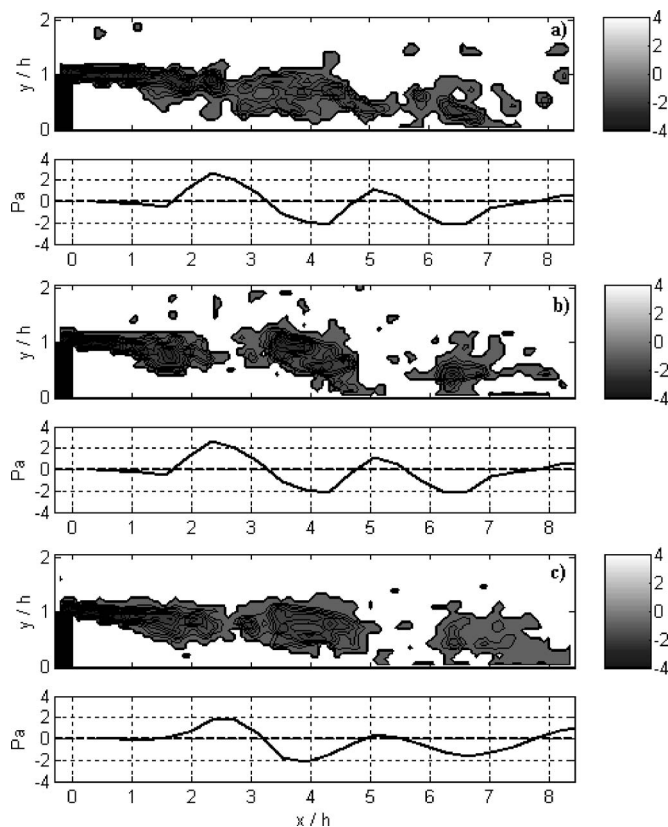

FIG. 23. Vorticity field at instant of acquisition of PIV image #67: (a) instantaneous, vorticity field, and pressure signature; (b) multipoint LSE using instantaneous, pressure signature; and (c) multipoint LSE using the first-four-POD-modes, pressure signature.

tures can be described using *only* the first four modes from the POD analysis.

To simplify the analysis of the pressure signature and allow for focus on the most dominant, spatial-pressure distributions, only the first four POD modes will be used to represent the wall-pressure fluctuations. As will be demonstrated later, the addition of the remaining modes does not alter the global, large-scale features of flow structures estimated from the surface-pressure data. Reconstruction of the pressure field using only the first four modes is accomplished by limiting the following summation (which recovers the full pressure field) to the first four terms:

$$p'(x,t) = a_1(t)\phi_1(x) + a_2(t)\phi_2(x) + a_3(t)\phi_3(x) + \cdots$$
$$+ a_{32}(t)\phi_{32}(x), \tag{5}$$

where $p'(x,t)$ is the instantaneous spatial wall-pressure signature and $a_1 - a_{32}$ are the amplitude coefficients for each of the mode functions, which are defined as $\phi_1 - \phi_{32}$. The pressure signature obtained using the first four terms in Eq. (5) will be combined with LSE to investigate the development of the large-scale structures associated with the dominant, organized component of the surface pressure.

Multipoint linear stochastic estimation (mLSE)

Multipoint, linear, stochastic estimation, which is an extension of the single-point LSE [Eqs. (1) and (2)], is given by

$$\tilde{u}' = A_{uo}p'(x_o,t) + A_{u1}p'(x_1,t) + A_{u2}p'(x_2,t) + \cdots$$
$$+ A_{un}p'(x_n,t), \tag{6}$$

$$\tilde{v}' = A_{vo}p'(x_o,t) + A_{v1}p'(x_1,t) + A_{v2}p'(x_2,t) + \cdots$$
$$+ A_{vn}p'(x_n,t), \tag{7}$$

where $A_{u0} - A_{un}$ and $A_{v0} - A_{vn}$ are the linear-estimation coefficients for each pressure point used in the LSE. For more detailed information, including how the coefficients are calculated, refer to Murray and Ukeiley[12] and references therein.

Figure 23 shows a comparison between an instantaneous, vorticity field at one instant in time (top plot), the

vorticity field estimated from the full, concurrent instantaneous, pressure signature (middle plot), and the vorticity field estimated from the portion of the same pressure signature recovered from the first four POD modes. The spatial, pressure signature is displayed below each vorticity field. The instantaneous, vorticity fields have been smoothed using a 3×3 filter in order to remove the effect of small-scale random turbulence and some of the noise resulting from calculating derivatives. The abscissa, the ordinate, and the gray-scale bar are the same as described in Fig. 18.

The selected time instant for the results shown in Fig. 23 is one where $p'(x)$ reflects an organized and energetic pattern. Figure 23(a) shows that at this time instant the flow field is dominated by large-scale concentrations of vortical structures. Three distinct structures can be identified near $x/h = 1.5$, 4, and 6.5. This distribution of the coherent structures in the flow field matches the instantaneous, pressure signature, which shows three local minima at the same streamwise positions. mLSE of the vorticity field in Fig. 23(b) shows a similar large-scale vortical distribution as seen in the instantaneous, vorticity field. The truncated POD representation [Fig. 23(c)] is also seen to give good representation of the large-scale vortex structures seen in the instantaneous, vorticity field. It is also seen in the latter that small-scale turbulence has been filtered out by the truncation, leaving only the large-scale structures needed for the analy-
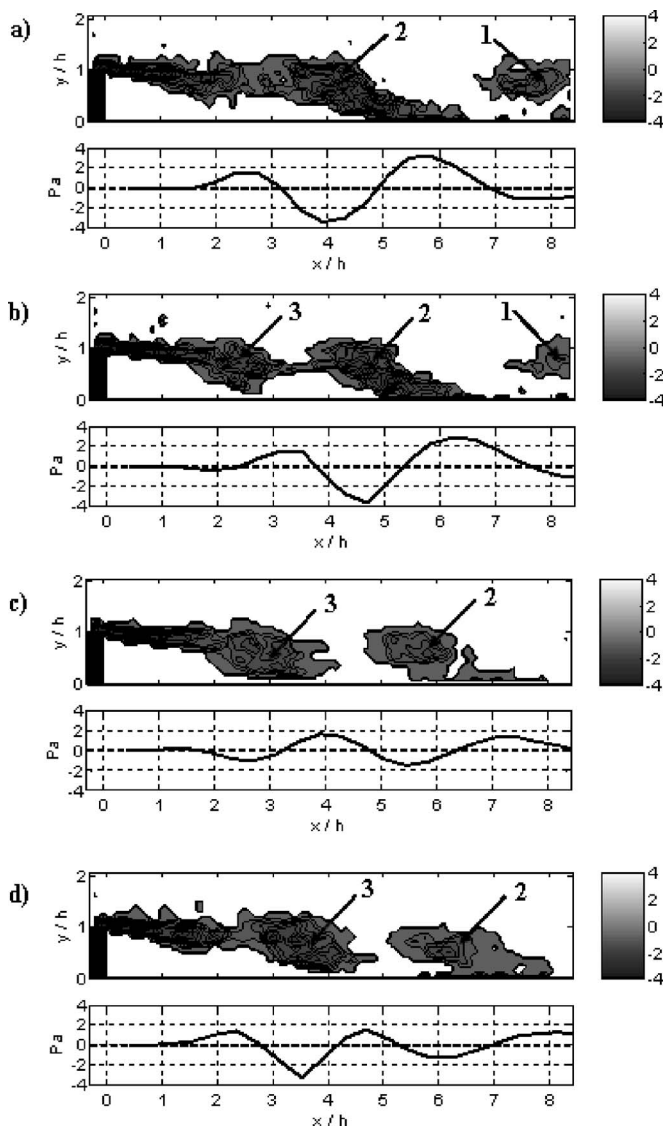
FIG. 24. Multipoint LSE of the vorticity field associated with the first-four-mode, pressure signature.

sis. It is important to note that Fig. 23 does demonstrate that mLSE is successful in obtaining a realistic representation of the *instantaneous* character of the large-scale, organized motions in the present flow field (rather than a smeared version, reminiscent of single-point estimations and conditional averages). However, it is not claimed here that mLSE yields an accurate *quantitative* flow estimation. The latter is not significant for the purposes of this study.

Figure 24 shows the evolution of the vorticity field using multipoint LSE based on the pressure signature of the first four modes. The abscissa and the ordinate give the streamwise and normal directions, respectively, normalized by the step height. The grayscale bar shows the magnitude of the nondimensional vorticity ($\omega_z^* = \omega_z h / U_\infty$), ranging from -4 to $+4$. The vorticity contours plotted are between -4 and -0.5 in an effort to clean up the plots by removing some of the background noise associated with the accuracy of evaluating the derivatives and to highlight regions dominated by high levels of vorticity. Beneath each contour plot is the mode-

pressure signature used to estimate the vorticity fields. The signature is given in pascals and is plotted as a function of streamwise distance. Numbers associated with arrows are used in the figure to identify coherent structures, which are defined as regions of vorticity concentration.

The sequence of events can be described starting with two coherent structures (1) and (2) in Fig. 24(a). Both convect farther downstream in Fig. 24(b), which is shown 2.1 ms after Fig. 24(a), while a concentration of vorticity (3) starts to form at streamwise location $x/h = 2$–3. The rollup of the large-scale vortex (3) continues 2.9 ms later in Fig. 24(c) and coherent structure (2) is seen to have moved farther downstream. It is interesting to note here that the streamwise extent between the two concentrations of vorticity (2) and (3) is equivalent to approximately $0.67x_r$. Cherry *et al.*[2] found the characteristic spacing between structures shedding from the reattachment zone to be between 60% and 80% of the separation bubble length. In Fig. 24(d), 6.25 ms later, coherent structure (3) increases in strength between $x/h = 3$–4 and at the same time the large-scale vortex (2) is decaying in the reattached boundary layer.

To get a more detailed look at the formation and subsequent evolution of the vortex structures, the results of Fig. 24 are replotted in Fig. 25 over a longer time period using a series of 36 plots of the vorticity field that are separated by a smaller time offset of 0.4 ms. The flow structure of interest in Fig. 25 is marked with an "*x*" by *visually* locating the highest vorticity value within the flow structure. Note that without the fitting of a curve to the vorticity distribution in order to locate the peak vorticity, a minimum uncertainty equal to the grid spacing of the PIV data (0.92 mm or 7.5% of the step height) is assumed in identifying the structure center. Additionally, the visual process of identification is likely to increase this uncertainty by a factor of 2 or 3. Therefore, it is estimated here that the identified structure location is known with 15%–20% uncertainty. Overall, detailed formation and subsequent evolution of the marked vortex structure is depicted in Fig. 25. To see this more clearly, the streamwise coordinate of the vortex is plotted as a function of time in Fig. 26. The figure shows the flow structure of interest remains stationary, within the uncertainty of the data, between $x/h = 2$–3 for the duration of the first 8–9 vorticity fields (≈ 3 ms) before it starts to accelerate downstream.

The picture drawn by the mLSE results of the dominant flow structures is quite consistent with the observations made from the wall-pressure and velocity-field statistics. For example, the idea of a large-scale vortex forming from the rollup of the thin shear layer, while the vortex remaining stationary between $x/h = 2$–3, is consistent with the sudden narrowing of $\mathbf{R}_{p'p'}$ (Fig. 7) and ballooning of the shear layer (e.g., Fig. 10) in the same x/h range. Furthermore, since acceleration is required for the formed, stationary vortex to travel downstream at some convection velocity, it is now clear why the surface-pressure, cross-correlation results reflect a convection velocity that increases with x, downstream of $x/h = 3$ (Figs. 8 and 15). It is noted here that this scenario is different from the commonly accepted view of the wall-pressure, generating mechanisms, where the vortex structures are viewed as gradually approaching the wall and growing in
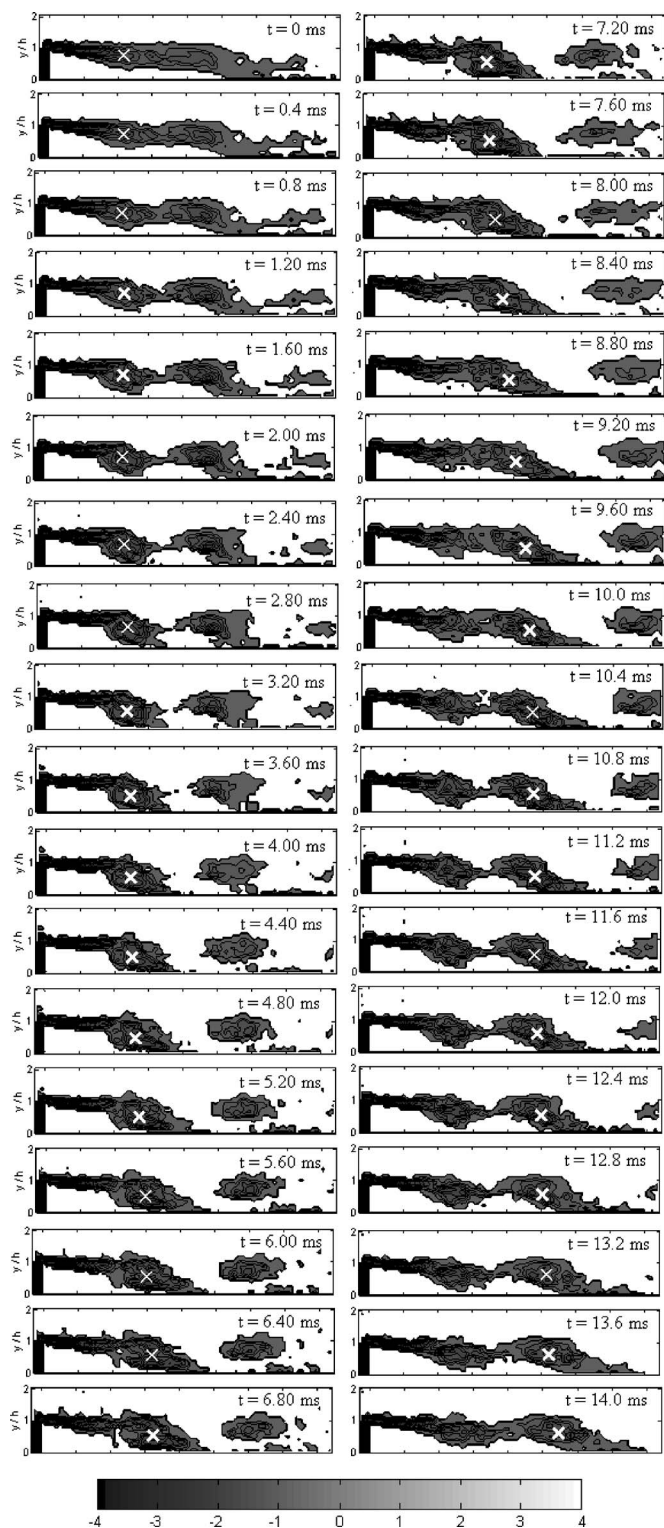
FIG. 25. Vorticity-field frames showing evolution of flow structure; time between successive frames, Δt, is 0.4 ms.
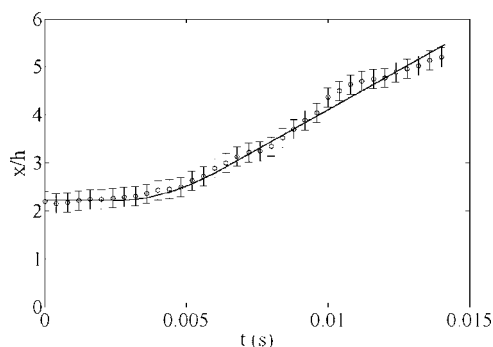

FIG. 26. Location of the flow structure identified in Fig. 25 vs time.

CONCLUDING REMARKS

The wall-pressure-based, mLSE analysis showed that a concentration of vorticity grows between $x/h = 2$–3 and reaches a height roughly equal to the step height before moving downstream. This finding provides an alternate view to the widespread view of the flow field downstream of a backward-facing step.

From literature, it is known that at the step edge, the turbulent boundary layer separates and forms a thin, shear layer. Due to Kelvin-Helmholtz instability, the shear layer rolls up to form small vortices of a size equivalent to the thickness of the shear layer. As the vortices continue to move downstream, they start to pair, triple, or even quadruple according to Smits,[35] who states that this appears to be the rapid growth mechanism in the shear layer. This initial rollup of the shear layer resembles the structure of a simple mixing layer as stated by Smits.[35] At approximately half of the reattachment distance, the small-scale structures continue to pair and form larger-scale, coherent structures. Smits[35] states that these coherent structures that are pairing continue downstream, roll around each other, and form a single, large-scale, vortical structure prior to reattachment.

The view discussed by Smits[35] corresponds to the widely accepted view of the BFS flow in which the growth of the shear layer structures occurs *spatially*; i.e., as the structures travel downstream. However, it can be seen in the present analysis that a large-scale, coherent structure actually forms while *remaining stationary* between $x/h = 2$–3. Figure 25 depicts this development of a large-scale coherent structure. In particular, it can be seen that a large-scale coherent structure grows in place (i.e., *temporally*) before reaching a height equivalent to the step height. At this point, the coherent structure sheds and by necessity *accelerates* to its ultimate convection speed in the downstream direction.

This temporal growth of the flow structures is similar to the development of the vortex structures in the wake of a bluff body (e.g., vortex shedding from a cylinder) than it is to a simple mixing layer. Therefore, to contrast the two view points, the scenario arrived at in this study will be referred to as "wake mode" versus the traditional one, which will be termed "shear-layer mode." It is important to realize that regardless of which of the two modes is prevalent, the flow structures ultimately grow to a scale of the order of the step height and they travel downstream with a certain convection
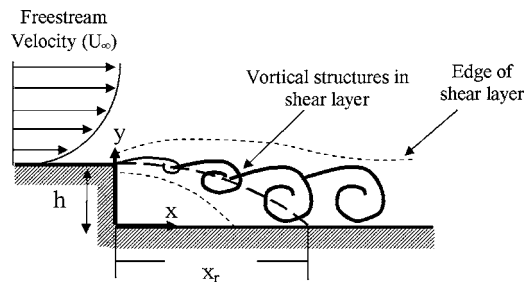
size as they travel downstream. Moreover, typically a single convection velocity is associated with these structures, or two or three values may be reported at different x locations without a clear reasoning for the physics underlying the observed variation.

FIG. 27. Idealized sketch of the flow structures development in "shear-layer mode" downstream of a backward-facing step.

FIG. 29. Streamwise distribution of the mean, streamwise velocity component at $y/h=0.05$.

velocity. Hence, the distinction of the two modes is likely to primarily affect the flow characteristics within the separation bubble rather than downstream of reattachment. Figures 27 and 28 provide an idealized sketch of the coherent structures developing in the separation bubble for the shear-layer and wake modes, respectively.

Only one other recent study indicates a scenario similar to that identified here. The study is conducted by Wee et al.[36,37] using a random vortex method, numerical simulation of the flow field downstream of a sudden expansion. Wee et al.[36,37] found that large-scale vortices periodically formed at the middle of the reattachment zone before shedding downstream. More interestingly, they also linked this temporal evolution of the structures downstream of the step to the existence of an absolute instability of the flow. Subsequent linear stability analysis showed that the location of maximum instability growth rate was found in the middle of the reattachment zone (in agreement with the location of formation of the vortices). Wee et al.[36,37] state that absolute modes are most likely to originate in a region with strongest backflow. In the present work, the backflow is strongest around $x/h=2$–3 ($U/U_\infty \approx -0.2$) as seen in the near-wall velocity plot in Fig. 29.

Huerre and Monkewitz[38] found that a two-stream mixing layer is absolutely unstable when the velocity ratio, defined as the velocity of one freestream divided by the velocity of another freestream, was less than −0.136. As shown in Fig. 29, the ratio of the maximum, reverse velocity to the freestream in this study has a value of $U/U_\infty \approx -0.2$ in the $x/h=2$–3 region, which is lower than the critical value found by Huerre and Monkewitz.[38] Thus, within this location, it is likely that an absolute instability exists, which leads to the rollup of the large-scale vortex. The absolute instability
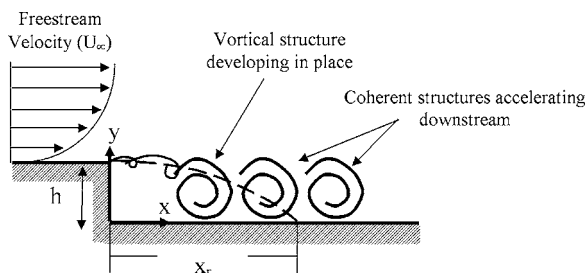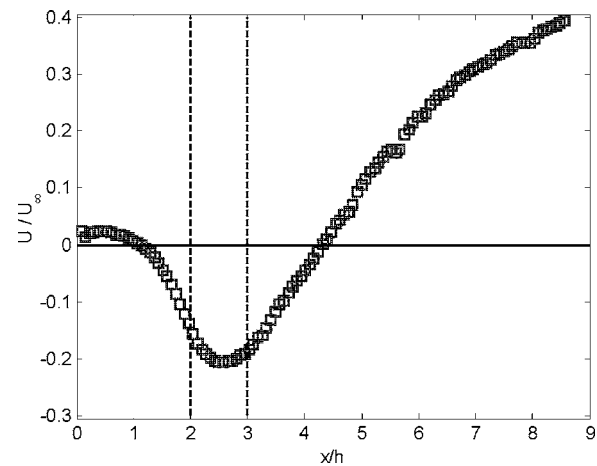
mechanism suggested by Wee et al.[36,37] and its relation to the formation of large-scale structures in the back-step flow are similar to the flow behavior in the wake of bluff bodies where the process of vortex shedding has been linked to the existence of an absolute-instability mechanism as well (Oertel[39]).

Strictly speaking, absolute instability is a concept that is tied to parallel flows (i.e., where the instability wavelength is much smaller than a streamwise length scale over which the flow field remains practically invariant). This clearly does not hold in the back-step flow (e.g., as pointed out earlier, the streamwise spacing of the vortex structures was found to be approximately 0.67 of the mean reattachment length). However, the temporal growth predicted by absolute instability is certainly consistent with observations of the unsteady flow structure. The reasons why absolute instability should work in a nonparallel flow situation are not clear. It is felt though, that the answer to this issue may come from some of the recent trends in stability analysis, where the global, rather than the local, behavior of the mean flow is considered in the calculation. Example studies of global instability analysis may be found in the review papers by Chomaz[40] and Theofilis.[41]

It is useful to note here that wake and shear-layer modes have in fact been identified in open-cavity flows since 1987 (Gharib and Roshko[42]). Moreover, a link between absolute instability and the wake mode has also been proposed in the cavity case (Rowley et al.[43]). Particularly interesting in the cavity flow case is that, with the exception of axisymmetric flow geometry (Gharib and Roshko[42]), observations of the wake mode remain confined to computational studies (Najm and Ghoniem[44] and Rowley et al.[43]). This could suggest that the observation of a wake mode may require idealized or close to idealized two-dimensional-flow geometry. This may provide a rationale for the commonly held belief that the vortical structures within the separation bubble develop as in a simple mixing layer rather than in a wake flow.

Finally, it is also important to note that the curvature of the axisymmetric model may also be linked to the observation of the wake mode. The initial shear-layer thickness from

FIG. 28. Idealized sketch of the flow structures development in "wake mode" downstream of a backward-facing step.

which the vortex structures develop is approximately $0.25h$ (see Fig. 13 near the step), and 5% of the radius of the model at separation. Whether the latter is small enough for curvature effects to be unimportant requires extension of the current study to include test models with different radii. Additionally, the azimuthal structure of the wake mode is not revealed in the present work. The recent study of Tinney *et al.*[45] in an axisymmetric, sudden expansion highlights the significance of helical modes $m=1$ and 2. This suggests that the wake mode found here may not be axisymmetric. Further measurements are required to address this issue.

ACKNOWLEDGMENTS

[1] J. K. Eaton and J. P. Johnston, "A review of research on subsonic turbulent flow reattachment," AIAA J. **19**, 1093 (1981).

[2] N. J. Cherry, R. Hillier, and M. E. M. P. Latour, "Unsteady measurements in a separated and reattaching flow," J. Fluid Mech. **144**, 13 (1984).

[3] I. P. Castro and A. Haque, "The structure of a turbulent shear layer bounding a separation region," J. Fluid Mech. **179**, 439 (1987).

[4] I. Lee and H. J. Sung, "Multiple-arrayed pressure measurement for investigation of the unsteady flow structure of a reattaching shear layer," J. Fluid Mech. **463**, 377 (2002).

[5] R. J. Adrian, "Conditional eddies in isotropic turbulence," Phys. Fluids **22**, 2065 (1979).

[6] T. C. Tung and R. J. Adrian, "Higher-order estimates of conditional eddies in isotropic turbulence," Phys. Fluids **23**, 1469 (1980).

[7] Y. G. Guezennec, "Stochastic estimation of coherent structures in turbulent boundary layers," Phys. Fluids A **1**, 1054 (1989).

[8] D. R. Cole and M. N. Glauser, "Applications of stochastic estimation in the axisymmetric sudden expansion," Phys. Fluids **10**, 2941 (1998).

[9] S. Stokes and M. Glauser, "Multi-point measurement techniques used in the study of separated flows," AIAA Pap. 99–3518 (1999), 30th AIAA Fluid Dynamics Conference, Reno, NV.

[10] A. M. Naguib, C. E. Wark, and O. Juckenhöfel, "Stochastic estimation and flow sources associated with surface pressure events in a turbulent boundary layer," Phys. Fluids **13**, 2611 (2001).

[11] J. Taylor and M. N. Glauser, "Towards practical flow sensing and control via POD and LSE based low-dimensional tools," J. Fluids Eng. **126**, 337 (2004).

[12] N. E. Murray and L. S. Ukeiley, "Estimation of the flowfield from surface pressure measurements in an open cavity," AIAA J. **41**, 969 (2003).

[13] C. E. Tinney, P. Jordan, J. Delville, A. M. Hall, and M. Glauser, "A time-resolved estimate of the turbulence and source mechanisms in a subsonic jet flow," AIAA Pap. 2006–621 (2006), 44th AIAA Aerospace Sciences Meeting and Exhibit, Reno, NV.

[14] J. P. Bonnet, J. Delville, and M. N. Glauser, "Coherent structures in turbulent shear flows: the confluence of experimental and numerical approaches," Proceedings of ASME FEDSM'02, FEDSM2002–31412, Montreal, Quebec, Canada, 14–18 July 2002.

[15] M. P. Wernet, "Fuzzy logic enhanced digital PIV processing software," 18th International Congress on Instrumentation for Aerospace Simulation Facilities (ICIASF), Toulouse, France, June 1999.

[16] J. F. Meyers, "Doppler global velocimetry—the next generation," AIAA Pap. 92–3897 (1992).

[17] M. P. Wernet, "Particle image velocimetry processing manual PIVPROC," Version 6.03, NASA Glenn Research Center, 2002.

[18] L. M. Hudy, A. Naguib, W. M. Humphreys, and S. Bartram, "Particle image velocimetry measurements of a two/three-dimensional separating/reattaching boundary layer downstream of an axisymmetric backward-facing step," AIAA Pap. 2005–0114 (2005), 43rd AIAA Aerospace Sciences Meeting and Exhibit, Reno, NV.

[19] T. M. Farabee and M. J. Casarella, "Measurements of fluctuating wall pressure for separated/reattached boundary layer flows," ASME J. Vib., Acoust., Stress, Reliab. Des. **108**, 301 (1986).

[20] A. F. Heenan and J. F. Morrison, "Passive control of pressure fluctuations generated by separated flow," AIAA J. **36**, 1014 (1998).

[21] D. M. Driver, H. L. Seegmiller, and J. G. Marvin, "Time-dependent behavior of a reattaching shear layer," AIAA J. **25**, 914 (1986).

[22] L. M. Hudy, A. M. Naguib, and W. M. Humphreys, Jr., "Wall-pressure-array measurements beneath a separating/reattaching flow region," Phys. Fluids **15**, 706 (2003).

[23] L. M. Hudy, "Simultaneous wall-pressure and velocity measurements in the flow field downstream of an axisymmetric backward-facing step," Ph.D. thesis, Michigan State University, 2005.

[24] F. Scarano and M. L. Riethmuller, "Iterative multigrid approach in PIV image processing with discrete window offset," Exp. Fluids **26**, 513 (1999).

[25] J. Kostas, J. Soria, and M. S. Chong, "Particle image velocimetry measurements of a backward-facing step," Exp. Fluids **33**, 838 (2002).

[26] R. Ruderich and H. H. Fernholz, "An experimental investigation of a turbulent shear flow with separation, reverse flow, and reattachment," J. Fluid Mech. **163**, 283 (1986).

[27] M. Raffel, C. Willert, and J. Kompenhans, *Particle Image Velocimetry: A Practical Guide*, 3rd ed. (Springer-Verlag, Berlin, 1998), p. 160.

[28] R. C. Cole, M. N. Glauser, and Y. G. Guezennec, "An application of the stochastic estimation to the jet mixing layer," Phys. Fluids A **4**, 192 (1992).

[29] J. P. Bonnet, J. Delville, M. N. Glauser, R. A. Antonia, D. K. Bisset, D. R. Cole, H. E. Fiedler, J. H. Garem, D. Hilberg, J. Jeong, N. K. R. Kevlahan, L. S. Ukeiley, and E. Vincendeau, "Collaborative testing of eddy structure identification methods in free turbulent shear flows," Exp. Fluids **25**, 197 (1998).

[30] L. Ukeiley and N. Murray, "Velocity and surface pressure measurements in an open cavity," Exp. Fluids **38**, 656 (2005).

[31] A. M. Naguib and M. M. Koochesfahani, "On wall-pressure sources associated with the unsteady separation in a vortex-ring/wall interaction," Phys. Fluids **16**, 2613 (2004).

[32] P. Bradshaw and Y. M. Koh, "A note of Poisson's equation for pressure in a turbulent flow," Phys. Fluids **24**, 777 (1981).

[33] J. L. Lumley, "The structure of inhomogeneous turbulence," in *Atmosphere Turbulence and Wave Propagation*, edited by A. M. Yaglom and V. I. Tatarsky (Nauka, Moscow, 1967), p. 166.

[34] G. Berkooz, P. Holmes, and J. L. Lumley, "The proper orthogonal decomposition in the analysis of turbulent flows," Annu. Rev. Fluid Mech. **25**, 539 (1993).

[35] A. J. Smits, "A visual study of a separation bubble," in Proceedings of the International Symposium on Flow Visualization, Bochum, Germany, 9–12 September 1980.

[36] D. Wee, S. Park, T. Yi, A. M. Annaswamy, and A. F. Ghoniem, "Reduced order modeling of reacting shear flow," AIAA Pap. 2002–0478 (2002), AIAA 40th Aerospace Sciences Meeting and Exhibit, Reno, NV.

[37] D. Wee, T. Yi, A. M. Annaswamy, and A. F. Ghoniem, "Self-sustained oscillations and vortex shedding in backward-facing step flows: Simulation and linear instability analysis," Phys. Fluids **16**, 3361 (2004).

[38] P. Huerre and P. A. Monkewitz, "Absolute and convective instabilities in free shear layers," J. Fluid Mech. **159**, 151 (1985).

[39] H. Oertel, "Wakes behind blunt bodies," Annu. Rev. Fluid Mech. **22**, 539 (1990).

[40] J.-M. Chomaz, "Global instabilities in spatially developing flows: non-normality and nonlinearity," Annu. Rev. Fluid Mech. **37**, 357 (2005).

[41] V. Theofilis, "Advances in global linear instability analysis of non-parallel and three-dimensional flows," Prog. Aerosp. Sci. **39**, 249 (2003).

[42] M. Gharib and A. Roshko, "The effect of flow oscillations on cavity drag," J. Fluid Mech. **177**, 501 (1987).

[43]C. W. Rowley, T. Colonius, and A. J. Basu, "On self-sustained oscillations in two-dimensional compressible flow over rectangular cavities," J. Fluid Mech. **455**, 315 (2002).

[44]H. N. Najm and A. F. Ghoniem, "Numerical simulation of the convective instability in a dump combustor," AIAA J. **29**, 911 (1991).

[45]C. E. Tinney, M. N. Glauser, E. L. Eaton, and J. A. Taylor, "Low-dimensional azimuthal characteristics of suddenly expanding axisymmetric flows," J. Fluid Mech. **567**, 141 (2006).